

# Intramuscular High-Density Micro-Electrode Arrays Enable High-Precision Decoding and Mapping of Spinal Motor Neurons to Reveal Hand Control

Agnese Grison<sup>1</sup>, Jaime Ibáñez Pereda<sup>1,2</sup>, Silvia Muceli<sup>1,3</sup>,  
Aritra Kundu<sup>1</sup>, Farah Baracat<sup>4</sup>, Giacomo Indiveri<sup>4</sup>,  
Elisa Donati<sup>4</sup>, Dario Farina<sup>1\*</sup>

<sup>1</sup>Department of Bioengineering, Imperial College London, London, United Kingdom.

<sup>2</sup>BSICoS group, I3A Institute and IIS Aragón, University of Zaragoza, Zaragoza, Spain.

<sup>3</sup>Department of Electrical Engineering, Chalmers University of Technology, Gothenburg, Sweden.

<sup>4</sup>Institute of Neuroinformatics, University of Zurich and ETH Zurich, Zurich, Switzerland.

\*Corresponding author(s). E-mail(s): [d.farina@imperial.ac.uk](mailto:d.farina@imperial.ac.uk);

## Abstract

Decoding nervous system activity is a key challenge in neuroscience and neural interfacing. In this study, we propose a novel neural decoding system that enables unprecedented large-scale sampling of muscle activity. Using micro-electrode arrays with more than 100 channels embedded within the forearm muscles, we recorded high-density signals that captured multi-unit motor neuron activity. This extensive sampling was complemented by advanced methods for neural decomposition, analysis, and classification, allowing us to accurately detect and interpret the spiking activity of spinal motor neurons that innervate hand muscles. We evaluated this system in two healthy participants, each implanted with three electromyogram (EMG) micro-electrode arrays (comprising 40 electrodes each) in the forearm. These arrays recorded muscle activity during both single- and multi-digit isometric contractions. For the first time under controlled conditions, we demonstrate that multi-digit tasks elicit unique patterns of motor

neuron recruitment specific to each task, rather than employing combinations of recruitment patterns from single-digit tasks. This observation led us to hypothesize that hand tasks could be classified with high precision based on the decoded neural activity. We achieved perfect classification accuracy (100%) across 12 distinct single- and multi-digit tasks, and consistently high accuracy ( $>96\%$ ) across all conditions and subjects, for up to 16 task classes. These results significantly outperformed conventional EMG classification methods. The exceptional performance of this system paves the way for developing advanced neural interfaces based on invasive high-density EMG technology. This innovation could greatly enhance human-computer interaction and lead to substantial improvements in assistive technologies, offering new possibilities for restoring motor function in clinical applications.

**Keywords:** motor neuron, motor unit, intramuscular EMG, myoelectric control

## 1 Introduction

Neural interface research aims to restore or establish connections between the nervous system and the external environment, for example in individuals with neurological impairments [1, 2]. These interfaces, based on stimulating (encoding) and/or recording (decoding) from neural pathways, are used to assist individuals with disabilities or enhance the capabilities of healthy individuals. For this purpose, the decoding of neural signals provides commands to virtual systems, wearable robots or tele-operated devices.

Direct brain signal decoding is the only option for severe impairments; however, for many other applications, nerve or muscle interfacing may be preferable [3, 4]. The surface electromyogram (EMG) is particularly simple to record and is used in several interfacing applications [5–7]. Although recording signals from muscle tissue is not a direct neural interface, the EMG captures the electrical activity produced by the muscles, which reflects the neural activation sent from the spinal cord’s output layers to the muscles [8]. Therefore, surface EMG signals can be decoded to reflect the activities of individual spinal motor neurons, which can then be mapped into estimated motor intent.

Despite the potential of surface EMG-based decoding of neural activity, current decoding and mapping systems are limited in accuracy and, particularly, vary significantly in performance across individuals and conditions. The primary cause of this variability is the dependence of surface EMG characteristics on the volume conductor separating the sources of signal (muscle fibers) and the recording electrodes. Associated to this limitation are the sensitivity of surface EMG features to electrode misplacement, typically due to donning and doffing of the wearable device [9], and EMG signal cross-talk [10, 11]. These and other limitations of wearable EMG sensors can be addressed with invasive electrodes. Recent advances in intramuscular EMG technology have provided micro-electrode arrays with tens of electrodes closely spaced with respect to each other (high-density EMG micro-electrode arrays) [12, 13].

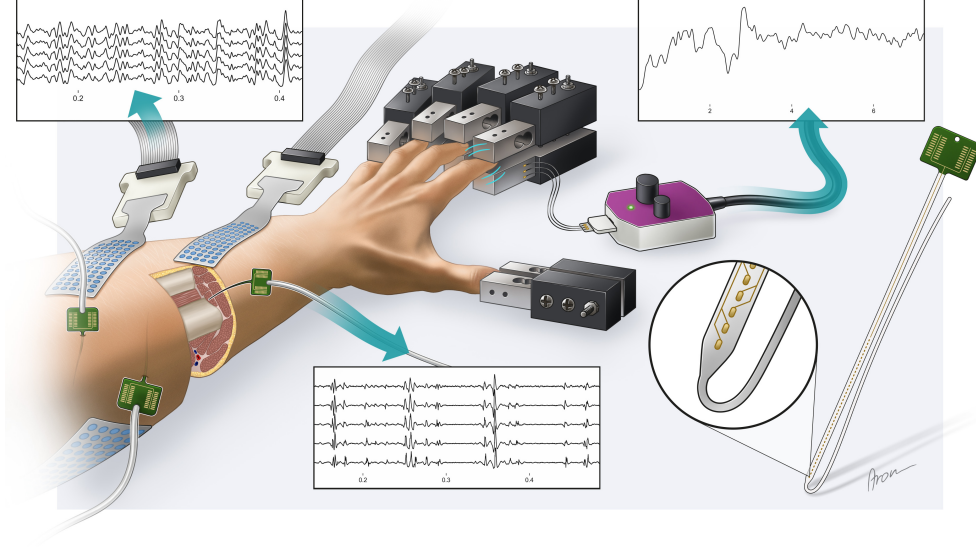


**Fig. 1** Experimental setup: Three micro-electrode arrays were implanted into the forearm muscles of two participants. Three high-density surface electrode grids were placed on the skin overlying the intramuscular recording sites. Two load cells per finger were used to measure flexion and extension forces. Representative data are shown for intramuscular EMG, surface EMG, and force recordings. A schematic of the high-density intramuscular micro-electrode arrays, with a detailed zoom-in on the electrode tip, is shown on the bottom right.

Here, we present an innovative neural decoding system that extracts neural information from high-density intramuscular EMG (HD-iEMG) micro-electrode array signals, mapping precise discharge timings of the decoded motor neurons into the executed tasks. This system was experimentally validated offline on two healthy individuals, using three concurrently implanted intramuscular electrodes in each subject (Fig. 1). The validation involved classifying single- and multi-digit isometric tasks. The performance of the HD-iEMG mapping was then compared to the use of traditional pattern recognition techniques applied to the high-density surface EMG (HD-sEMG) and HD-iEMG signals. Therefore, we present four key advances in the field of neural decoding: 1) recordings of 120 intramuscular signals concurrently detected, paired with corresponding HD-sEMG signals. This is so far the largest reported number of implanted electrodes in the forearm muscles; 2) new perspectives on the neural command structure underlying finger movements; 3) a highly accurate neural classifier (100% accuracy in single- and multi-digit tasks for 12 classes), using physiological and interpretable features; 4) a comprehensive comparison of mapping performance across invasive and non-invasive high-density recording modalities. These findings enhance our understanding of neuromuscular control of the hand and have significant implications for neuroprosthetics and human-machine interfaces.

## 2 Results

### 2.1 Targeted muscle insertions

The recording of multiple high-density intramuscular data arrays represents one of the key innovations of this study. HD-iEMG enables recordings from a significantly larger number of sites compared to traditional needle or wire electrode arrays [14]. Furthermore, HD-iEMG signals exhibit greater spatial and temporal sparsity than HD-sEMG, allowing for more precise analysis of motor neuron activity [13]. In this study, three HD-iEMG electrodes were inserted in the forearm muscles of two healthy participants, with one electrode placed in each of the most relevant extrinsic muscles for finger flexion and extension. Interfacing with motor units that control hand function poses inherent challenges due to the precise targeting required for intramuscular electrode placement in the primary muscles responsible for dexterous control. Optimal electrode placement sites were determined via a magnetic resonance imaging (MRI)- and ultrasound-based anatomical assessment of the forearm. MRI was employed to gain a detailed understanding of the forearm muscle anatomy and to guide the insertion point and angle of the electrodes. Specific forearm points were tracked using MRI markers across scans, allowing precise localization of marker positions and detailed insights into forearm structure (Fig. 2 a). Each electrode array, comprising 40 platinum electrodes ( $140\ \mu\text{m} \times 40\ \mu\text{m}$ ) linearly distributed over 2 cm with 0.5 mm inter-electrode (IED) spacing [13], targeted muscles involved in finger movements. The insertion of each array was facilitated by a 25-gauge hypodermic needle, which was attached to the electrode with a guiding filament. Once the electrode was positioned, the filament was cut, allowing the needle to be removed while the electrode remained securely in the muscle.

The first micro-electrode array targeted the extensor pollicis longus (EPL) and extensor digitorum communis (EDC) muscles, activated for the extension of the thumb and the digits respectively. A distal location in the forearm was chosen to allow concurrent monitoring of the two muscles. The second array was inserted transversely to target the extensor digiti minimi (EDM) and the extensor digitorum communis (EDC), employing an unconventional technique that represents a novel approach to intramuscular electrode placement, thereby maximizing coverage of the muscles relevant to digit extension. The third array targeted the flexor digitorum superficialis (FDS) muscle, chosen for its accessibility and essential role in flexion tasks.

MRI provides a comprehensive anatomical view of the forearm, but practical constraints limit its use during needle insertions. Once the electrode insertion points and general positioning were identified using MRI, precise muscle targeting during the actual insertion became essential to avoid veins, arteries, and nerves. This necessitated real-time imaging guidance to ensure accurate and safe insertion. A portable ultrasound device (Butterfly iQ+) was used to precisely visualise electrode paths to target muscles in real-time (Fig. 2 c and d, for Subject 1 (S1) and Subject 2 (S2), respectively). Post-insertion, subjects performed maximal muscle contractions (MVC) as reference for submaximal tasks. This procedure also confirmed secure electrode placement and minimised the risk of displacement.



While electrode placement followed the above rigorous procedure, some errors in the exact target placements occurred. For example, the limited field of view of the ultrasound probe impeded the full tracking of the micro-electrode array targeting the EDM for both subjects (panels **c**, **d**, second column). The extension of the insertion to the boundary of the Extensor Carpi Radialis Brevis (ECRB) suggests that the electrode might not have fully targeted the EDM, potentially failing to record specific information related to the little finger tasks. Moreover, although the EPL was targeted in both subjects (panels **c**, **d**, first column), the number of channels within the muscle was relatively small (panels **c**, **d** first column). This potentially impacted the amount of information recorded from the EPL during these tasks. The micro-electrode arrays were acutely implanted in the target muscles with percutaneous wires.

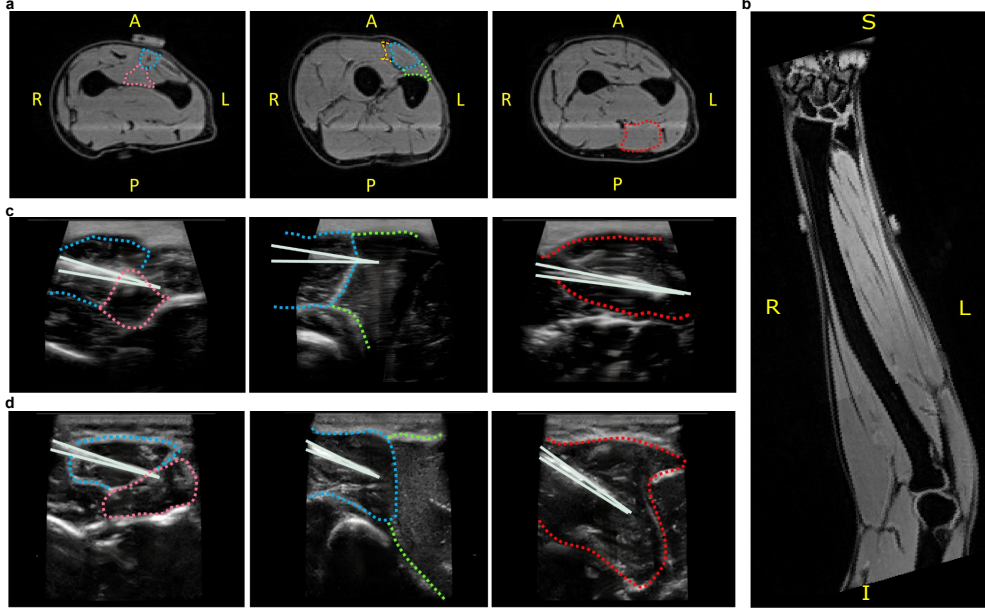


**Fig. 2** MRI and ultrasound images of the forearm with the boundaries of the relevant muscles highlighted in color (EPL: pink, EDC: blue, EDM: orange, ECRB: green, FDS: red). **a** MRI scans of the forearm of one subject with highlighted boundaries of the targeted muscles. The first MRI image includes a marker for precise positioning within the forearm's anatomical structure. **b** Detailed MRI view of the forearm. **c**, **d** Ultrasound image during the micro-electrode array insertion for subject S1 (**c**) and subject S2 (**d**). The guiding needle is highlighted in white.

## 2.2 Data characteristics

Concurrent recordings of HD-iEMG and HD-sEMG were obtained during flexion and extension tasks for each finger of the hand individually and for four combinations of finger tasks. By accurately decoding the electrical activity into the spiking activities of spinal motor neurons, we uncovered distinct neural signatures associated with each

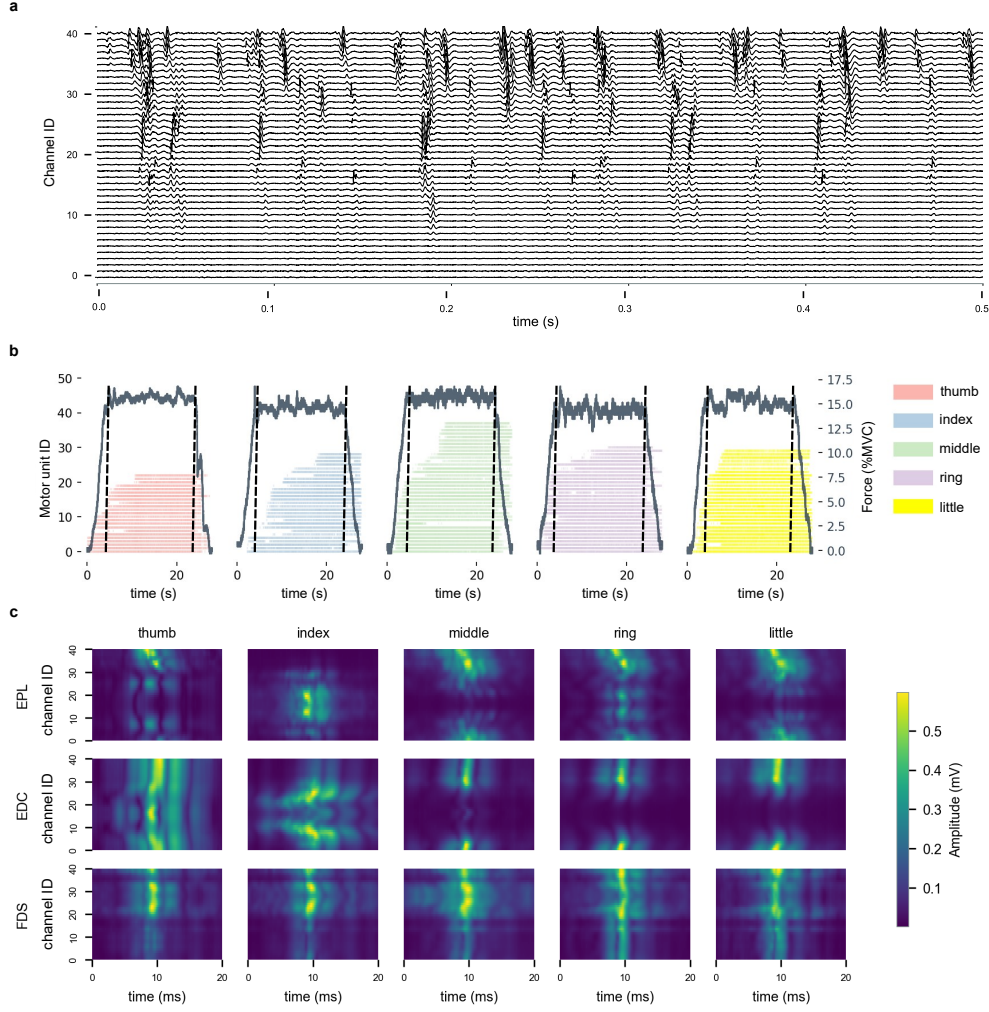
task, providing deeper insights into the neural mechanisms underlying fine motor control. Leveraging this new understanding, we then performed classification analyses across multiple conditions, further validating the robustness of these task-specific neural patterns. First, we classified 16 classes of gestures, which included all individual finger movements and three two-finger combinations, in both flexion and extension. Next, we analysed the 12 classes that corresponded to tasks primarily controlled by the implanted muscles, ensuring that these tasks involved movements whose neural activity was captured by the intramuscular micro-electrode arrays. Finally, as a proof of concept for prosthetic hand control (one representative application of this mapping system), we selected eight functionally relevant tasks, which are challenging to decode with current methods (see Section 4.1.2 in Methods for more details).

Figure 3 **a** shows a representative example of the data recorded from one of the micro-electrode arrays within the muscle. The multi-channel data recorded from all three micro-electrode arrays was subsequently decomposed to identify the spiking times of individual motor units (Fig. 3 **b**). On average,  $27.1 \pm 12.9$  (S1) and  $8.0 \pm 6.1$  (S2) motor units were identified from the HD-iEMG per task (mean and std across two repetitions, the three electrodes, and the 16 tasks). The average discharge rate of the decomposed motor units across the two participants was  $11.0 \pm 3.9$  spikes/s. Figure 3 **c** presents the average amplitude maps of motor unit activation during different finger extension tasks. These maps were generated by first computing the spike-triggered average for each motor unit action potential, per electrode, and per task, followed by normalisation and rectification. The spike-triggered averages were then averaged across all active motor units for each electrode and task to highlight the areas of the electrode array that were most active for each task. As shown in Figure 3 **c**, the electrodes exhibited task-specific activity, indicating localised activation within each array. This observation reflects the high spatial selectivity of each HD-iEMG channel. While some improvements in insertion procedures may be needed in future studies, the results indicated that the recorded information was of high quality for the subsequent analyses.

### 2.3 Neural control of digit tasks

This study marks the first instance in which we have been able to sample a relatively large number of motor neurons across multiple single- and multi-digit tasks under standardized conditions. By analyzing the activities of these motor neurons, we uncovered distinct neural patterns associated with different tasks, enhancing our understanding of the neural mechanisms underlying fine motor control.

Figure 4 shows the distribution of active motor units for individual finger movements and three two-finger combinations, with flexion tasks in panel **a** and extension tasks in panel **b**. Tasks are arranged along the axes, with bold squares highlighting motor units engaged during the specific task. The data reveal that the highest number of active motor units were consistently task-specific. Motor units active during other tasks are shown using distinct colors and patterns—solid colors for flexion and diagonal hatching for extension—facilitating comparisons of motor unit engagement across different movements. While some motor units were engaged during other



**Fig. 3** **a** A 0.5-second segment of HD-iEMG data captured during the extension of the little finger from the EPL electrode. **b** Raster plots showing the extension movements of individual fingers for the second repetition for subject S1. The sections within the dashed lines indicate the parts of the signal considered for this study. **c** Average amplitude map of motor unit activities during the extension task of each finger and for each electrode (S1). The x-axis represents time in ms, and the y-axis represents the 40 channels recorded per electrode.

tasks, their contribution was minor compared to the dominant task-specific activity, emphasizing the precision and task-specific recruitment of motor units. Notably, motor units involved in single-digit tasks were rarely recruited for multi-digit tasks involving the same finger. On average, motor units from single-digit tasks contributed for only  $2.3 \pm 3.7\%$  of the motor units recruited across all multi-digit tasks and movement directions, underscoring the specialized recruitment of motor units for multi-digit

movements. Furthermore, motor units that were active across all tasks, but not specifically tied to the task in focus, contributed for  $44.6 \pm 11\%$ , though task-specific motor unit activity consistently accounted for the majority of the recruitment. These findings highlight the nuanced and highly selective recruitment patterns of motor units during complex hand movements.

Figure 4 c provides a representative example of motor unit action potential waveforms for index flexion (blue), middle flexion (green), and the combination of index and middle finger flexion (pink). The distinct waveform shapes between the combination and individual finger movements visually confirm, for this representative example, that mostly unique motor units were activated for each task. This suggests that specific motor units are recruited in different patterns depending on the complexity and nature of the finger movements. The ability to distinctly identify these patterns is crucial for accurate decoding and mapping systems. The distinct activation of motor units for each task suggests that this decoding system is well-suited for highly accurate gesture classification. This consistency supports the use of motor unit activity to reliably differentiate gestures, as explored in the subsequent classification analysis.

## 2.4 Decoding hand function

The following sections present the results of three offline analyses: 1) classification of all 16 classes of recorded tasks; 2) classification of a subset of 12 classes associated to tasks primarily requiring the muscles that were targeted by the multi-electrode arrays (see Section 2.1), and 3) classification of six (S1) and eight (S2) classes chosen as important for prosthetic control [15] (considered as a potential application of the proposed decoding system). In all analyses, results are reported when using three feature spaces: motor unit discharge timings as decoded from HD-iEMG, root mean square (r.m.s.) values for each channel of the HD-iEMG, and r.m.s. values for each channel of the HD-sEMG. The different classification pipelines are depicted in Figure 5. Additionally, in the first two analyses we report results from lower-density iEMG and sEMG signals (in Figure 6 b and d respectively). This analysis was performed to investigate whether high-density configurations were essential for achieving high prediction accuracy.

### 2.4.1 Full classification (16 classes)

In the analysis of motor tasks spanning all 16 flexion and extension categories, the motor neuron discharge timings decoded from HD-iEMG provided a perfect classification accuracy for subject S1 of 100% and an accuracy of 96.1% for subject S2 on average across the tasks. The mis-classification for subject S2 was exclusively related to the little finger, and it was due to the fact that the electrode placement did not adequately target the EDM, the muscle primarily responsible for the activation of the little finger. The accuracy using the decomposition from the HD-iEMG recordings was higher than that achieved using the r.m.s. values of the HD-iEMG (90.1% and 94.3%) or the r.m.s. values of the HD-sEMG (96.6% for S1, 76.5% for S2). Figure 7 presents the confusion matrices per subject and classification type.

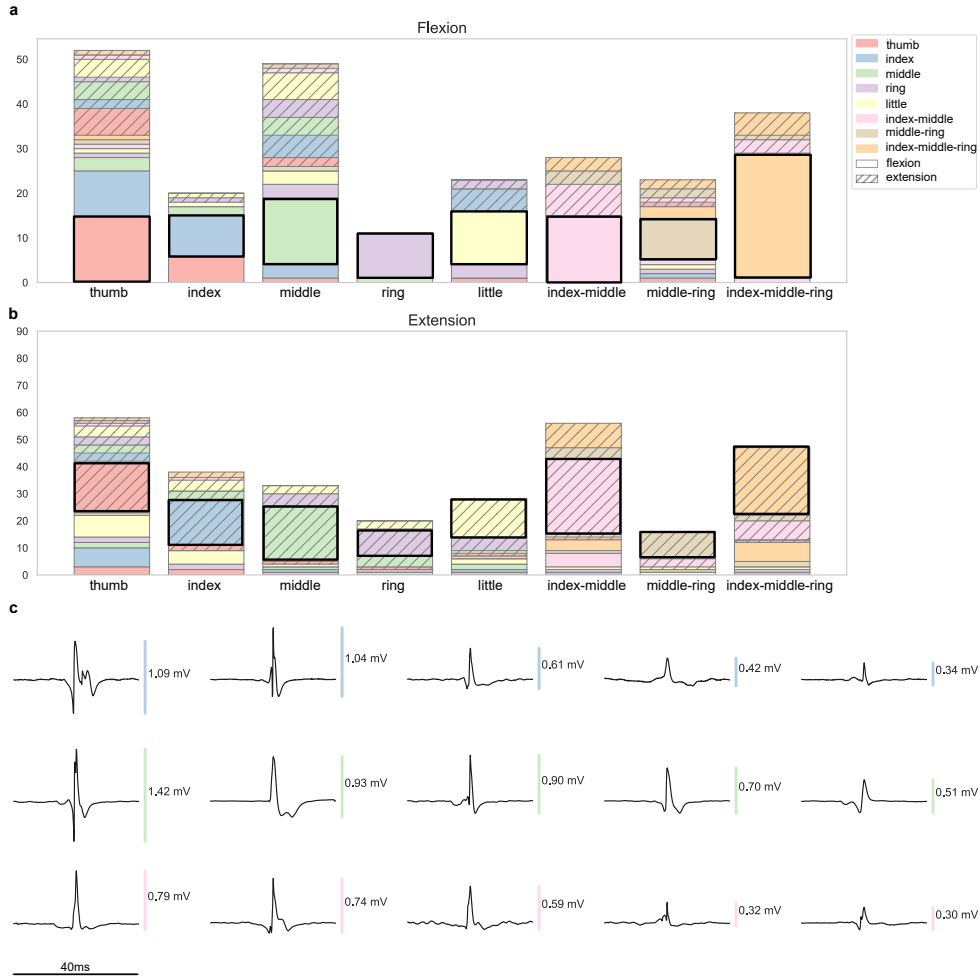


**Fig. 4** Motor unit counts for S1 during flexion (a) and extension (b) tasks classified from the 16 classes. Each bar represents the number of motor units that were active during the specific task, labelled according to the filter that produced the accepted source. The hatch pattern distinguishes the extension task from the flexion task, providing a clear visual differentiation between the two movements. This highlights the distribution and activity levels of motor units across different tasks. c Representative motor unit action potentials decomposed from the FDS electrode for S1 during various tasks: index finger flexion (blue), middle finger flexion (green), and the combination of index and middle finger flexion (pink). The majority of the motor units in the combination task originate from unique MUs specific to the combined movement, rather than being a combination of the motor units active during the individual index and middle finger flexion tasks. This indicates distinct motor unit recruitment patterns for the combined task compared to the individual tasks.

#### *Lower-density electrode configurations*

When using low-density EMG configurations, the accuracy decreased substantially compared to the high-density systems, with the bipolar intramuscular achieving 47.8% for S1 and 69.0% for S2, and the sEMG achieving 92.5% for S1 and 64.3% for S2. These

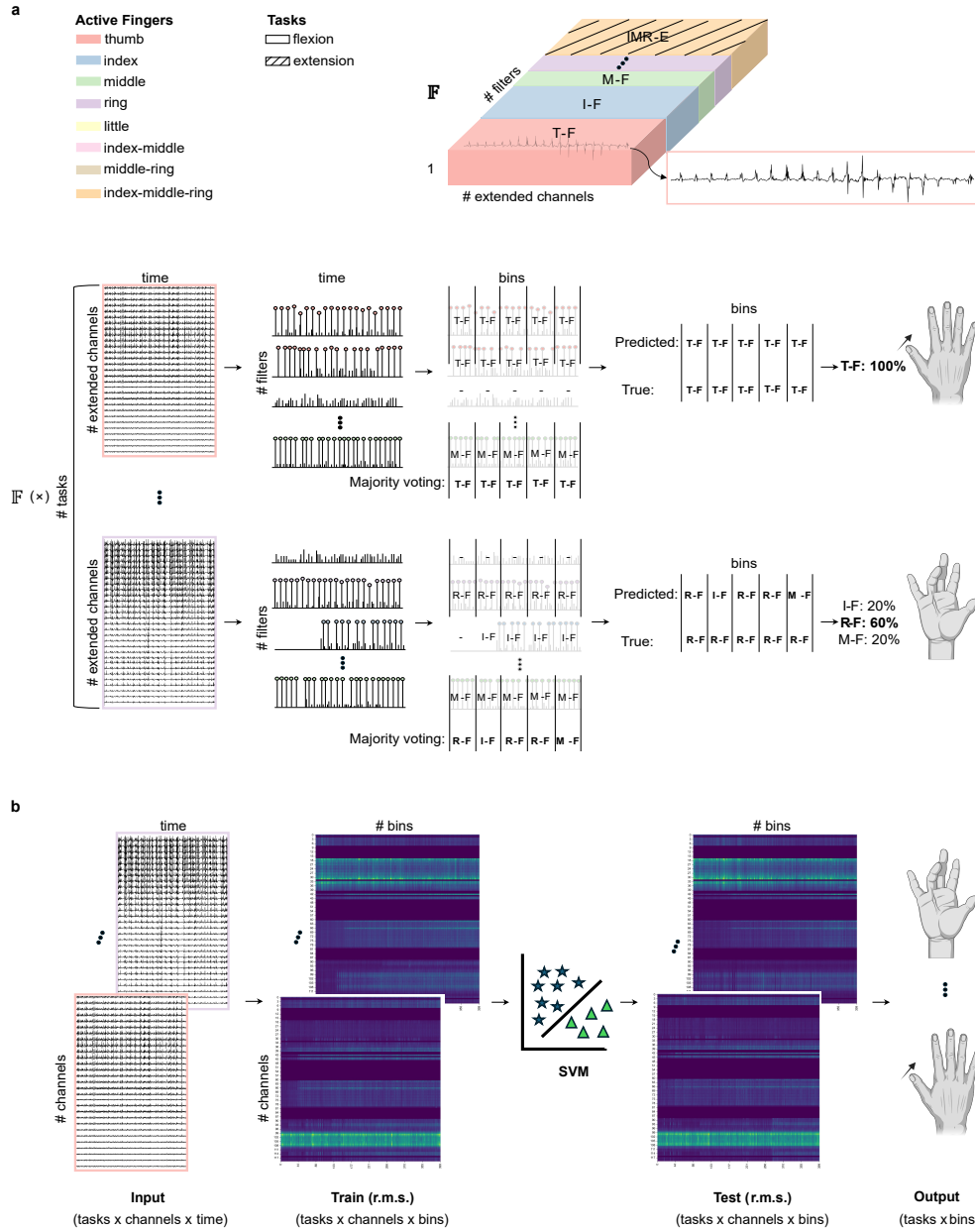


**Fig. 5** Analysis pipelines. **a** Classification using the MU discharge times as features. The EMG signals from each task (finger flexion and extension) were decomposed into individual motor unit activities. The motor unit action potential filters were then pooled into a filter bank, denoted as **F**. These filters were applied to the EMG signals of each task, generating a set of Innervation Pulse Trains (IPTs). Each IPT was clustered into source and noise components. If the clustering quality was robust, the source was accepted and segmented into sliding windows. Each time bin was assigned a class label based on the filter that produced the corresponding source. Majority voting was applied across the set of IPTs for each segment. The final classification label was determined by the ratio of correctly labelled segments to the total number of labelled segments. **b** Classification from global EMG features. The r.m.s. values of the EMG signals were extracted and segmented into sliding windows. These formed the input to a linear C-Support Vector Machine (SVM) classifier. The model was fit on the training data and then applied to the test data for classification. The resulting output provided the final classification labels.

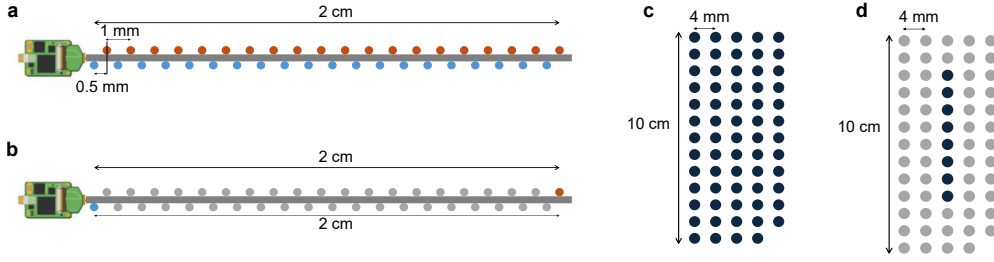


**Fig. 6** The four electrode configurations considered in this study. **a** HD-iEMG electrode, 40 channels with 0.5 mm IED. **b** Lower-density iEMG electrode, two channels with 2 cm IED. **c** HD-sEMG electrode, 64 channels with 4 mm IED. **d** Lower-density sEMG electrode, eight channels with 4mm IED.

results indicate that the reduction in accuracy when shifting from a high-density to a lower-density configuration for pattern recognition is particularly large for intramuscular recordings and more modest for surface signals [16, 17]. The confusion matrices for the bipolar and low-density sEMG signals are shown in Appendix B, Figure B1.

#### 2.4.2 Targeted muscle classification (12 classes)

Figure 8 shows the confusion matrices for the classes fully captured by the electrodes, as confirmed by ultrasound imaging (Fig. 2). The classifier using motor units decomposed from HD-iEMG signals reached 100% accuracy for both S1 and S2, which shows a perfect classification when targeting all muscle structures responsible for the tasks. The classifier using r.m.s. values from HD-iEMG achieved an accuracy of 99.3% for S1 and 99.7% for S2, while the classifier using r.m.s. values from HD-sEMG reached an accuracy of 95.3% for S1 and 71.4% for S2.

These results underscore the superior performance of intramuscular configurations over surface configurations for the classification based on neural features. When the electrodes accurately targeted the relevant muscles, the classification accuracy was 100% in the two subjects.

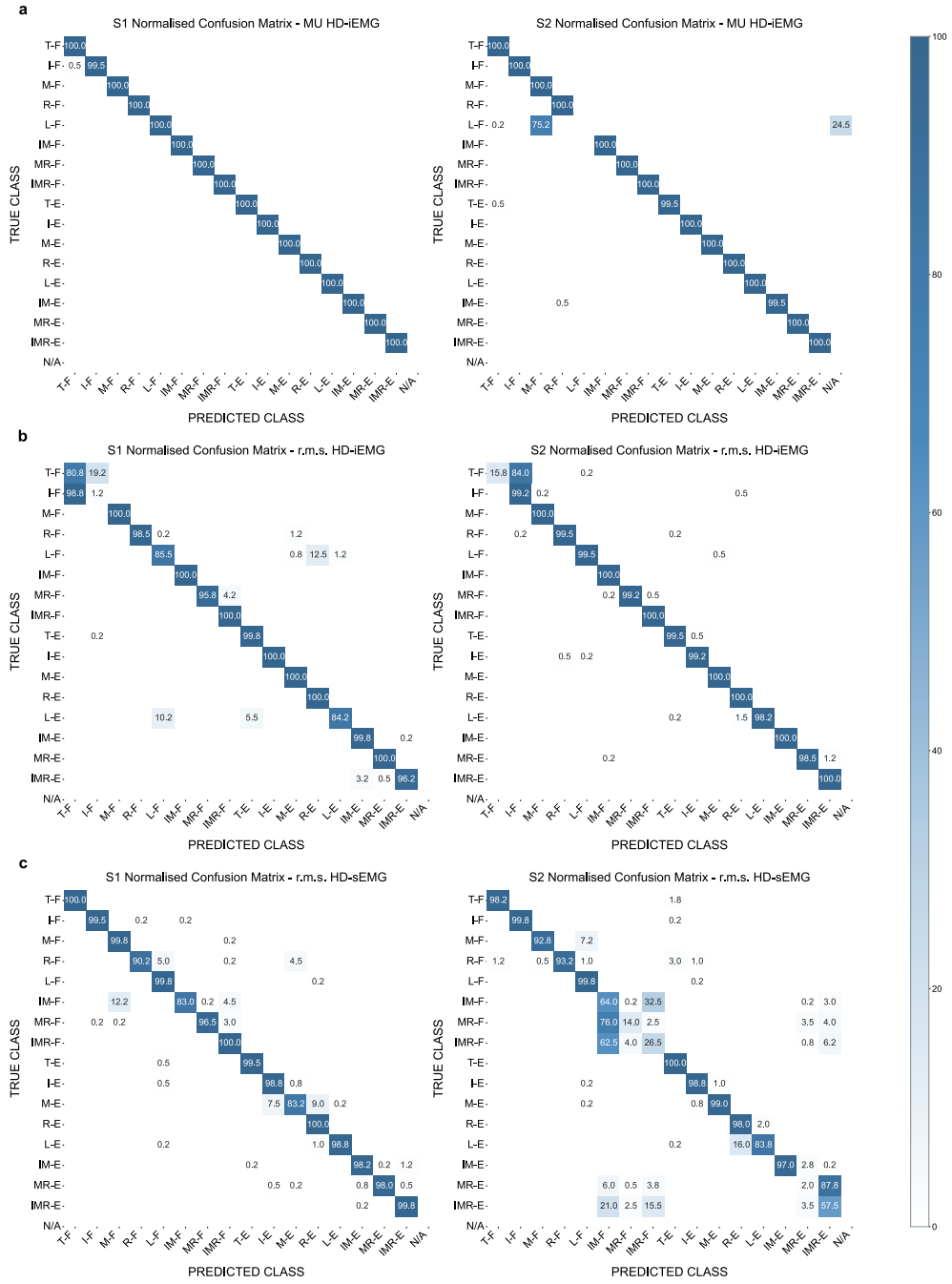
##### *Lower-density electrode configurations*

On average across the two subjects, the bipolar iEMG achieved an accuracy of 55.4% for S1 and 78.8% for S2, while the sEMG achieved an accuracy of 89.1% for S1 and 57.2% for S2. These results show a notable reduction in the accuracy compared to the high-density configuration systems, highlighting the importance of a high-density setup in achieving high classification accuracy. The confusion matrices for the 12-class classification from the lower-density configurations are shown in Appendix B, Figure B2.

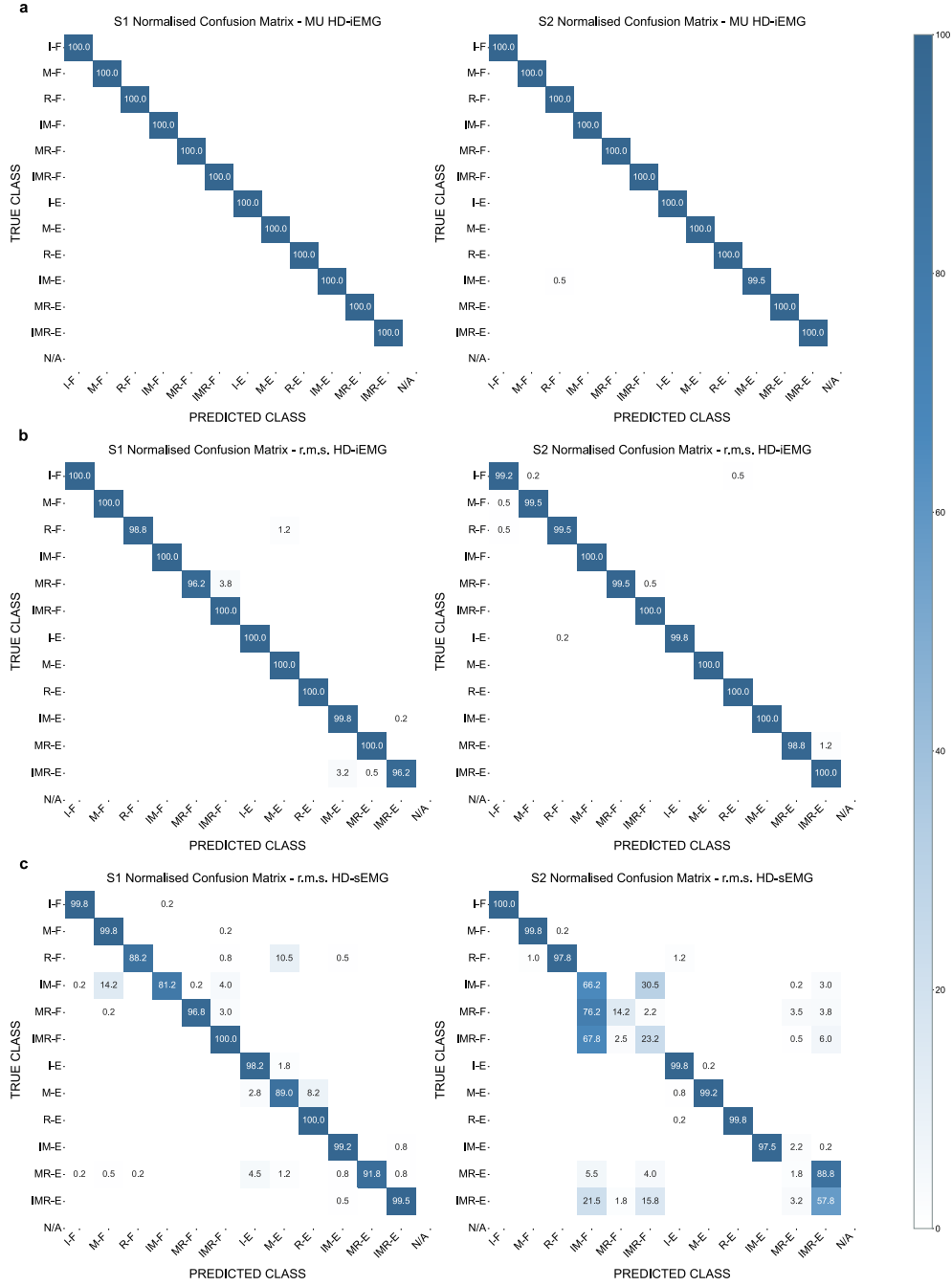
#### 2.4.3 Mapping specific functional classes (6 and 8 classes)

Figure 9 presents the classification results when focusing on the classes most relevant from a control perspective. Results are reported for six (S1) and eight (S2) classes (refer to Methods for details). The accuracy achieved from the motor unit activities decoded





**Fig. 7** Normalised confusion matrices illustrating the percentage of predictions for each of the 16 flexion and extension gestures, comparing true labels (y-axis) with predicted labels (x-axis). MU stands for motor unit. The matrices show predictions for S1 on the left and S2 on the right, across different data types: **a** HD-iEMG motor units. **b** r.m.s. values of HD-iEMG. **c** r.m.s. values of HD-sEMG.



**Fig. 8** Normalised confusion matrices illustrating the percentage of predictions for each of the 12 flexion and extension gestures, comparing true labels (y-axis) with predicted labels (x-axis). MU stands for motor unit. The matrices show predictions for Subject S1 on the left and S2 on the right, across different data types: **a** HD-iEMG motor units. **b** r.m.s. values of HD-iEMG. **c** r.m.s. values of HD-sEMG.

from HD-iEMG was 99.4% for S1 and 100% for S2, while the accuracy from the r.m.s. values of the HD-iEMG was 76.4% for S1 and 89.0% for S2. The accuracy from the r.m.s. values of the HD-sEMG was 87.0% for S1 and 74.4% for S2. The effectiveness of using high-density intramuscular EMG recordings combined with MU decomposition for neural prosthesis control is demonstrated also in this analysis by the very high accuracy rates (>99%). This near-perfect accuracy in classifying gestures typically used for prosthetic hand control indicates the potential of the proposed interface in external device control.

### 3 Discussion

Decoding motor intent is critical for accurate control in neural interfacing systems. At the peripheral level, decoding performance depends heavily on the type and quality of recorded muscle signals. We developed an advanced intramuscular neural system capable of decoding the precise discharge timings of spinal motor neurons by deconvolving HD-iEMG recordings. These recordings capture detailed neural signals from motor neuron pools, offering rich insight into underlying motor control processes. The proposed system allowed us to observe motor neuron recruitment in single- and multi-digit tasks, revealing that a majority of motor units recruited during each task are task-specific, even when the same digits are used. These insights into motor neuron behavior suggest a strong potential for precise discrimination between hand tasks, which our system successfully validated with high accuracy.

Our recording and decoding system allowed us to explore the neural control during digit tasks. Notably, we observed that the motor units recruited during multi-digit tasks were almost entirely distinct from those recruited during the tasks of the corresponding single digits. This finding aligns with previous research by Oßwald et al. [18], which also suggested that motor unit recruitment during multi-digit tasks is well separated from that of single-digit tasks; however, this previous study was limited by the unconstrained and dynamic nature of the tasks investigated. Our results strongly indicate that hand control in multi-digit tasks is characterized by maximal separation of degrees of freedom, likely due to the demands of dexterous control. This was evidenced by the count of motor units active per task (Fig. 4). Additionally, we provided representative examples of the distinct action potential waveforms associated with different tasks, further supporting the highly specific recruitment of motor units during single- vs multi-digit tasks.

Building on this understanding of the neural mechanisms underlying fine motor control, we hypothesized that a system leveraging the decoded activities of motor neurons could achieve near-perfect accuracy in gesture classification. This is because the detection of task-specific motor units is a perfect indicator of a task. The accuracy of the proposed mapping system was validated through a series of experiments. A novel signal classification method was applied to the decoded series of discharge timings, achieving near-perfect discrimination for six, eight and 12 classes (average >99%), and up to 16 classes (average >96%). While traditional HD-iEMG and HD-sEMG features demonstrated solid performance (over 71%), the motor neurons identified through HD-iEMG consistently yielded superior accuracy, exceeding global features by 0.3%

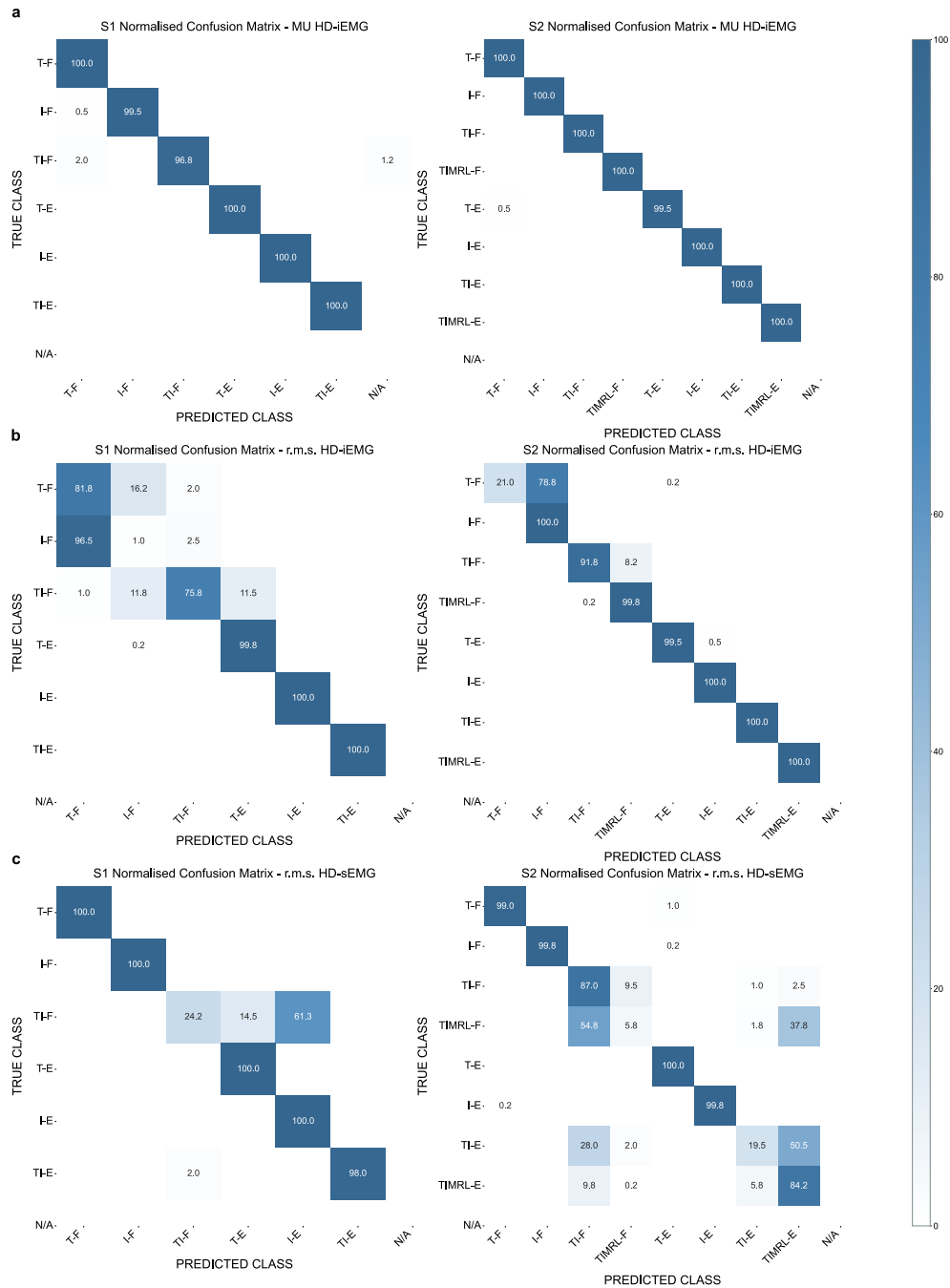


**Fig. 9** Normalised confusion matrix illustrating the percentage of predictions for each of the six (S1) and eight (S2) flexion and extension gestures, comparing true labels (y-axis) with predicted labels (x-axis). MU stands for motor unit. **a** motor unit HD-iEMG. **b** r.m.s. values of HD-iEMG **c** r.m.s. values of HD-sEMG.

to 28.6%, depending on the conditions. The substantial improvement in classification accuracy is highly relevant for applications in neuroprosthetics, as this increase in accuracy can significantly enhance the effectiveness and responsiveness of assistive devices, leading to better user experiences and outcomes. Moreover, in all tasks, the classification accuracy from HD-iEMG motor units for the combined finger movements approached 100% (Figs. 7 a, 8 a), further validating the task-specific recruitment of motor units during multi-digit tasks.

Decoding motor intent can be approached through global EMG features or motor unit discharge timings, each with distinct advantages and challenges. Global EMG features represent the spatiotemporal convolution of many motor neuron discharges but are variable across individuals, particularly when recorded at the skin surface. This variability, alongside issues like amplitude cancellation and cross-talk, complicates precise control in complex tasks [19, 20]. Due to these challenges, global HD-sEMG achieved classification accuracies ranging from 71% to 97%, highlighting variability in performance across tasks.

Although relatively high classification accuracies were achieved in some tasks, the reliance on features that are not directly linked to the underlying physiological mechanisms diminishes interpretability and presents challenges for clinical applications and motor control research. Understanding the specific contributions of muscle groups and neural activity is essential for validating model predictions and enhancing practical utility. In contrast to global EMG features, motor neuron discharge timings provide a direct and physiologically relevant representation of neural activity, closely reflecting the spinal-level coding mechanisms of movement. By decomposing the EMG signals into their constituent motor unit activities, we demonstrated that motor neuron spike trains can serve as critical sources of information for identifying complex tasks. This approach addresses the variability present in global EMG by separating neural information from muscle fiber action potentials, ensuring that the shapes of action potentials do not influence classification outcomes. Additionally, this separation mitigates the effects of EMG amplitude cancellation and enhances spatial and temporal sparseness, thereby reducing issues related to cross-talk [21].

A key novelty of this work is the recording of high-density data intramuscularly, enabling detailed and accurate decoding of neural activity. The importance of intramuscular measurements is underscored by the large number of motor units that could be decomposed per task. High-density surface EMG has also been used for motor unit decoding [8] but it presents evident limitations with respect to implanted systems. One of these limitations is that it typically allows for the decoding of fewer motor units. This limitation is compounded by the challenge of accurately determining which muscles are activated, primarily due to a lack of spatial selectivity in the signals captured. This lack of resolution can lead to overlapping activity from adjacent muscles, making it difficult to pinpoint specific muscle contributions during movement [19, 20].

Precise targeting of the appropriate muscles and decoding of direct neural information resulted in nearly perfect decoding accuracy from the motor unit activity derived from HD-iEMG. Ensuring accurate muscle targeting remains critical for effectively extracting useful information from these recordings. As we reported in Section 2.4.2, when there was high confidence in the targeted muscles, the accuracy of classification from decoded motor unit activities was 100%.

Lower-density configurations were extracted from the high-density iEMG and sEMG data to evaluate whether multi-channel configurations were necessary for achieving high classification accuracies. The results showed that classification accuracy from global EMG features dropped with fewer channels, more significantly so for the iEMG. Regarding the 16 class classification, the bipolar iEMG configuration dropped by 40% for S1 and by 25% for S2 for 16 classes, while sEMG dropped by 4% for S1 and just over 10% for S2. A similar trend was observed for the 12 classes. This highlights the importance of high-density configurations to accurately classify gestures from the EMG. It is important to note that classification based on motor neurons would not be feasible with lower-density configurations, as high-density setups are essential for the decomposition methods utilised to extract motor neuron activity.

Various approaches have been explored in previous research for classifying hand gestures from global EMG features. For eight classes, time domain and deep learning methods have shown variable level of success, with accuracies ranging from 81.54% [22] to 95% and about 91% [23]. A convolutional auto-encoder combined with a CNN achieved 99% accuracy for 10 finger gestures [24], but this approach was tested on a smaller set of 10 classes compared to the 16 and 12 classes used in our study.

There have also been previous studies that presented results on classification of motor unit activities, extracted from surface EMG, associated to hand tasks. For example, neural drives to muscle regions were estimated by grouping motor neurons based on the spatial location of their corresponding muscle units, achieving over 97% accuracy across 11 classes in patients with targeted nerve reinnervation [8], while similar methods using motor unit action potential waveform activations reached around 95% accuracy for 11 classes [25]. A related technique employing motor unit filters achieved 94.6% accuracy for 12 gestures [26]. Additionally, neuromorphic approaches have shown promise, with approximately 95% accuracy for 10 classes [27].

Overall, our method outperforms all previous approaches, achieving accuracies exceeding 99% for six, eight, and 12-class classification tasks and greater than 96% for 16 classes. Notably, the precision obtained from motor unit activity significantly surpasses prior results, highlighting the robustness and reliability of our system for decoding neural information. The use of motor units not only enhances performance but also provides a theoretical framework for achieving 100% accuracy. As long as motor unit discharges are accurately detected, and each task involves at least one unique motor unit, it becomes theoretically possible to reach perfect classification. This implies that, with precise muscle targeting and continued advancements in decoding algorithms, flawless performance is achievable — a potential we have already demonstrated in some cases in this study (e.g., 100% accuracy for both S1 and S2 in the 12-class classification).

Under the experimental conditions of our study, the proposed approach based on decoding motor neurons demonstrated superior accuracy compared to traditional pattern recognition methods. However, the small sample size, driven by the need for intramuscular insertions, limits the generalization of these results. Further validation with a larger population is needed.

Transitioning to online implementation for real-world applications presents significant challenges. Real-time HD-iEMG decomposition is computationally intensive,

requiring high sampling frequencies to capture neural signals accurately [28]. While advances in microprocessor speeds have made real-time neural data processing more attainable, the challenge remains significant due to the intensive computational demands, especially since even offline data recordings are often hindered by the high sampling rates required (this problem is clearly exacerbated when increasing the number of channels, as in this study).

A promising future direction is the integration of spiking neural networks directly onto low power mixed-signal neuromorphic chips [29, 30]. As decomposition methods continue to advance and become more capable of adapting to signal nonstationarities [31], implementing real-time decomposition methods with neuromorphic electronic circuits will significantly accelerate the development of practical neural interfaces. The combination of adaptive signal processing and the computational efficiency of neuromorphic architectures represents a crucial step toward deploying neural prosthetics and other neurotechnologies that rely on real-time neural decoding [32]. This integration would not only enhance the system’s ability to handle dynamic, real-world scenarios but also reduce the need for constant retraining.

Despite the clear advantages of intramuscular systems over non-invasive ones, practical challenges hinder their widespread adoption. Precise muscle targeting is essential, requiring careful planning and execution by trained personnel. Mis-targeting can lead to mis-classifications, while increasing the number of electrodes could improve targeting accuracy. Our study focused on well-controlled isometric contractions, where signal decomposition is highly reliable. The system remains untested in dynamic, naturalistic conditions where movement alters action potential shapes.

In conclusion, we have described new findings on the motor control of multi-digit tasks. Additionally, we have proven the possibility of decoding the behaviour of the pools of motor neurons that physiologically innervate some of the muscles responsible for finger movements. This decoding was demonstrated in two healthy individuals with three implanted electrodes each and was shown to provide information that can be used for highly intuitive and accurate control commands. The accuracy of control derived from motor units extracted from HD-iEMG was near-perfect for both subjects and was successfully tested across a range of conditions, encompassing six to 16 distinct fine finger gestures.

## 4 Methods

### 4.1 Data Acquisition

#### 4.1.1 Participants

Two healthy men, aged 39 and 30 years, were recruited for this study. Both participants had no history of neurological or musculoskeletal disorders that could affect motor neuron functionality. The small subject sample was due to the relatively complex implant procedure, which included three micro-electrode arrays per subject, with ultrasound-guided insertion (see below). All experimental procedures adhered to the ethical guidelines set by Imperial College London. The studies were performed according to the Declaration of Helsinki, with an informed consent form signed by all participants



before each experiment (ICREC Project ID 19IC5640 for the intramuscular recordings; JRCO Project ID 18IC4685 for the MRI acquisition).

#### 4.1.2 Experiments

HD-iEMG signals were recorded from forearm muscles using multi-channel intramuscular electrodes designed for acute recordings [12, 13] (Fig. 6 a). Additionally, three surface electrode grids (IED 4mm) with 64 recording sites each (Fig. 6 c) were positioned over the targeted muscles to concurrently acquire HD-sEMG signals. This configuration enabled concurrent measurement of the electrical activity both within the muscle and at the skin surface. The EMG signals were acquired using a multi-channel amplifier (OT-Bioelettronica, Torino, Italy). All EMG data were sampled at 10,240 Hz, and digitised with 16-bit resolution. The HD-EMG signals were bandpass filtered (Butterworth, order 5) between 100-4400 Hz (HD-iEMG) and 20-500Hz (HD-sEMG). Recordings were made in bipolar configuration with a reference electrode placed on the wrist.

The participants performed force-tracking tasks following trapezoidal force trajectories at 15 % of their MVC (Fig. 3 b). These tasks were executed individually for each finger (thumb, index, middle, ring, and little finger) in flexion and extension. Additionally, forces were exerted by combinations of fingers (thumb and index; index and middle; middle and ring; index with middle and ring; thumb with index, middle, ring, and little finger) in flexion and extension, following the same trapezoidal profile. During all tasks, participants maintained isometric contractions focusing on the specified movements. The duration of the constant-force part of the contractions was 20 seconds. Two repetitions were recorded for each task.

A total of 20 types of contractions (classes) were performed. In the following, these classes were labelled as follows: thumb flexion (T-F), index flexion (I-F), middle flexion (M-F), ring flexion (R-F), little flexion (L-F), thumb and index flexion (TI-F), index and middle flexion (IM-F), middle and ring flexion (MR-F), index and middle and ring flexion (IMR-F), thumb and index and middle and ring and little flexion (TIMRL-F) thumb extension (T-E), index extension (I-E), middle extension (M-E), ring extension (R-E), little extension (L-E), thumb and index extension (TI-E), index and middle extension (IM-E), middle and ring extension (MR-E), index and middle and ring extension (IMR-E), thumb with index, middle, ring, and little extension (TIMRL-E).

We classified the different tasks with a series of analyses. First, we attempted the classification of 16 classes that included all individual fingers in flexion and extension, and three combinations of two fingers (T-F, I-F, M-F, R-F, L-F, IM-F, MR-F, IMR-F, T-E, I-E, M-E, R-E, L-E, IM-E, MR-E, IMR-E). Then, we focused on the tasks mostly associated to the targeted muscles, which resulted in 12 classes: I-F, M-F, R-F, IM-F, MR-F, IMR-F, I-E, M-E, R-E, IM-E, MR-E, IMR-E. Finally, as a proof of concept of a specific application of the mapping system - the control of a prosthetic hand - we selected tasks that are functionally important for amputees and challenging to decode with state-of-the-art methods [15, 33]. This group of tasks included power grip (TIMRL-F, TIMRL-E), pinch (TI-F, TI-E), and individual index/thumb finger activation (T-F, T-E, I-F, I-E), for a total of eight classes. All tasks were performed isometrically, with the corresponding fingers activated simultaneously. However, the

power grip class was excluded for subject S1 due to the inability to correctly perform the coordinated movements of the thumb, index, middle, ring, and little fingers. Specifically, S1 exhibited oscillations in the force applied by the little finger, with fluctuations of amplitude of around 7 %MVC. These force variations led to inconsistent activation of the motor units, which were subsequently removed by the automatic cleaning process. As a result, the last analysis resulted in six classes for S1 (T-F, I-F, TI-F, T-E, I-E, TI-E) and eight for S2 (T-F, I-F, TI-F, TIMRL-F, T-E, I-E, TI-E, TIMRL-E).

#### 4.1.3 Instrumented platform

A finger force measurement platform was designed to be adaptable to different hand sizes, adjustable in wrist angle, and equipped with high-resolution and cost-effective load cells to capture force signals. A 10-mm polycarbonate board was used for the platform body because of its light weight. Precision laser-cutting of load cell rails was executed using CAD software. The platform features ten 10-kg TAL220 load cells (two per finger, one for flexion, and one for extension), selected based on the maximum observed male exertion forces of 7-8 kg [34, 35]. The load cells are mounted on adjustable rails with rolling pins and connected to 3D-printed mounts to accommodate varying finger thicknesses. The EMG signals and the force data were acquired simultaneously by the Quattrocento amplifier. Force signals were amplified using Forza pre-amplifiers linked to the amplifier. A 3D-printed holder housed the 10 pre-amplifiers, optimising the setup for accurate force measurement across various hand sizes.

## 4.2 Classification

We examined the accuracy in classifying intended motor tasks into predefined categories by comparing two approaches: one that used decomposed motor unit activity (i.e., the timings of motor neuron discharge events) and another that used global features derived from the interference signal (e.g., signal amplitude).

To classify tasks using motor neuron behaviour, the HD-iEMG signals were decomposed into the contributing motor units. The filters associated with each source (motor unit) were aggregated into a comprehensive dictionary of filters for each task. Figure 5 panel **a** provides a schematic representation of this filter bank. In the diagram, each colour corresponds to a different class label, indicating the specific task being represented. The width of each bar reflects the number of filters associated with that task, illustrating how many motor unit filters contribute to the classification of each specific task. The zoomed-in section within the magenta box offers a closer look at a representative filter from the pooled filter bank. This filter visualises the amplitude of the motor unit across different channels, providing insights into how the neural activity is distributed spatially across the electrode array. Conversely, for global EMG classification, the root mean square of the EMG signals served as the feature for a C-Support Vector Machine classifier (Fig. 5 **b**). To mimic a real-life mapping system, the calibration phase was conducted using the first recorded repetition, and the testing phase was performed using a repetition recorded later in the day.

#### 4.2.1 Finger task classification based on motor unit behaviour

Motor unit spike trains were extracted through blind source separation of HD-iEMG recordings obtained during isometric finger tasks at 15 %MVC (see Appendix A for more details on EMG decomposition). The tasks included individual finger flexion and extension as well as multi-finger combinations performed isometrically. The decomposition process produced task-specific sets of motor unit filters, which were pooled to create a comprehensive bank of motor unit action potential filters  $\mathbf{F}_i \in \mathbb{R}^{N \times M}$ , where  $N$  represents the total number of extracted motor unit filters and  $M$  the number of EMG channels. Each motor unit filter  $\mathbf{F}_i$  in this set was labelled according to the specific finger movement task it was derived from (e.g., thumb flexion corresponding to class 0).

These reference motor unit filters from the 15 %MVC contraction were then applied to the multi-channel iEMG signals  $\mathbf{E}j \in \mathbb{R}^{M \times D_R}$ , where  $D_R$  is the duration of the recording, recorded during a separate 15 % MVC trial involving all fingers performing both flexion and extension movements. This produced the corresponding discharge timings, represented as IPTs  $\mathbf{I}ij \in \mathbb{R}^{N \times D_R}$  for each motor unit  $i$  and task  $j$ . Each IPT  $\mathbf{I}ij$  was clustered to separate the peaks (i.e., the source) from the noise components. Only motor units with robust clustering quality (silhouette value  $>0.9$ ), physiological discharge periodicity (coefficient of variation  $<35\%$ ), and firing rates within the physiological range for isometric contractions (mean discharge rate  $<30$  Hz) were retained for further processing. The discharge timings of these units were temporally segmented into 100-ms time bins with 50% overlap. This window was selected to be long enough for reliable classification while remaining short enough to minimize delay in real-time control applications. The windowing resulted in a binary matrix  $\mathbf{B} \in \mathbb{R}^{N \times K}$ , where  $K$  represents the number of bins. For each time bin  $k$ , the corresponding class label was assigned according to the filter  $\mathbf{F}_i$  that produced the source, creating a final label vector  $\mathbf{L} \in \mathbb{R}^K$ . If no predictions were made for a given bin (i.e., no motor units were active), it was labeled as N/A. Finally, for each time bin, the class with the majority of votes was assigned to that bin. If there were no predictions overall for a bin, it was labeled as N/A and counted as a misclassification in the final accuracy calculation. The method, therefore, relies on unique motor units being consistently active throughout the entire task. Figure 5 a shows a schematic of the method.

#### 4.2.2 Finger classification based on global EMG

For myoelectric decoding of dexterous hand gestures, a linear SVM classifier with an L2 regularisation penalty factor of 0.1 was employed (Fig. 5 b). The SVM classifier is a widely used method in EMG pattern recognition [36–38]. The HD-EMG signals were bandpass filtered (Butterworth, order 5) between 100-4400 Hz (HD-iEMG) and 20-500 Hz (HD-sEMG) to remove noise. Global normalisation factors based on the maximum absolute value across the pooled training set were derived and applied to the test set for consistent scaling. Outlier channels with baseline noise exceeding 3 standard deviations from the training mean were removed from all training and testing data. The pre-processed EMG was segmented into 100-ms intervals, with 50% overlap using a sliding window, preparing the bins similarly to how they were organised for the classification based on motor units. The r.m.s. values of the EMG were extracted

as the input features. This was done in the same way for both surface and intramuscular high-density recordings. Moreover, to simulate a lower-density iEMG electrode configuration, we selected the first and last channel for each electrode, resulting in an IED of 2 cm (Fig. 6 b). The difference between the two electrodes was computed for each array, resulting in 3 feature channels. This configuration was chosen to emulate structures like the implantable myoelectric sensors (IMES) electrodes, currently being tested to control multifunction hand prostheses [39–41]. For the surface electromyography (sEMG), we selected eight channels in the central column of the electrode grid, mimicking the configurations found in commercial low-density systems such as the MYOband (Fig. 6 d).

## 5 Acknowledgments

We thank the participants who generously contributed their time and effort to this study. We also thank Fabio Bolognesi for his help with the synchronization of the force and EMG recordings.

A.G. was supported by UK Research and Innovation [UKRI Centre for Doctoral Training in AI for Healthcare grant number EP/S023283/1] and by Huawei Technologies Research & Development (UK) Limited. J.I.P. was supported by project ECHOES (ERC Starting Grant 101077693), by a Consolidación Investigadora grant (CNS2022-135366) funded by MCIN/AEI/10.13039/ 501100011033 and UE’s NextGenerationEU/PRTR funds. S.M. was supported by Chalmers Life Science Engineering Area of Advance. A.K. was supported by NISNEM (EPSRC EP/T020970/1). D.F. was supported by NaturalBionicS (ERC Synergy 810346).

## 6 Conflict of interest

N/A

## 7 Ethics approval and consent to participate

All experimental procedures adhered to the ethical guidelines set by Imperial College London. The studies were performed according to the Declaration of Helsinki, with an informed consent form signed by all participants before each experiment (ICREC Project ID 19IC5640 for the intramuscular recordings; JRCO Project ID 18IC4685 for the MRI acquisition).

## 8 Data availability

The data that support the findings of this study are available from the corresponding author (D.F.) upon reasonable request.

## 9 Code availability

The code developed to analyse the data is available from the corresponding author (D.F.) on request.

## 10 Author contribution

A.G., J.I.P., S.M., D.F. conceptualized the study. A.G., J.I.P., A.K., S.M., D.F. performed the experimental measures. A.G. performed the data analysis. F.B., E.D., G.I. provided guidance to the project. A.G., D.F. prepared the first draft of the manuscript. All authors edited the manuscript for important scientific content and all approved the final version.

## 11 Consent for publication

N/A

## Appendix A Decomposition

The EMG signals were decoded into the discharges of the corresponding motor units via a blind source separation algorithm [42].

Multi-channel EMG signals represent combined mixtures of motor neuron spike trains. Each recorded signal, i.e., each EMG channel, is the summation of the convolution of unknown finite impulse response filters, corresponding to a motor unit action potentials, with their respective sources, i.e., the sequences of motor neuron discharge timings. To make the deconvolution (i.e., *EMG decomposition*) possible, this combined mixture can be converted into a linear instantaneous mixture by extending the sources to include the original  $n$  sources and their delayed versions, with delays ranging from 1 to the filter length  $L$ . Similarly, the  $m$  original observations are extended by a factor  $R$  to ensure there are more observations than sources [43].

For each time sample ( $k$ ), indicating the sources, observations and noise, respectively, with  $\underline{s}(k) = [s_1(k), s_2(k), \dots, s_n(k)]^T$ ,  $\underline{x}(k) = [x_1(k), x_2(k), \dots, x_m(k)]^T$  and  $\underline{n}(k) = [n_1(k), n_2(k), \dots, n_n(k)]^T$ , where  $T$  is the transpose operator, the extended model is as follows:

$$\underline{\tilde{x}}(k) = [\underline{\tilde{H}}\underline{\tilde{s}}(k) + \underline{\tilde{n}}(k)] \quad \text{for } k = 1, \dots, D_R \quad (\text{A1})$$

where  $D_R$  is the duration of the recording in samples, and with the extended sources, observations and noise as  $\underline{\tilde{s}}(k) = [\underline{\tilde{s}}_1(k), \underline{\tilde{s}}_2(k), \dots, \underline{\tilde{s}}_n(k)]^T$ ,  $\underline{\tilde{x}}(k) = [\underline{\tilde{x}}_1(k), \underline{\tilde{x}}_2(k), \dots, \underline{\tilde{x}}_m(k)]^T$  and  $\underline{\tilde{n}}(k) = [\underline{\tilde{n}}_1(k), \underline{\tilde{n}}_2(k), \dots, \underline{\tilde{n}}_n(k)]^T$ , where:

$$\begin{aligned} \underline{\tilde{s}}_j(k) &= [s_j(k), s_j(k-1), \dots, s_j(k-L-R)] & j &= 1, \dots, n \\ \underline{\tilde{x}}_i(k) &= [x_i(k), x_i(k-1), \dots, x_i(k-R)] & i &= 1, \dots, m \\ \underline{\tilde{n}}_i(k) &= [n_i(k), n_i(k-1), \dots, n_i(k-R)] & i &= 1, \dots, m \end{aligned}$$

The mixing matrix representing the filters is:

$$\widetilde{H} = \begin{bmatrix} \widetilde{h_{11}} & \cdots & \widetilde{h_{1n}} \\ \vdots & \ddots & \vdots \\ \widetilde{h_{m1}} & \cdots & \widetilde{h_{mn}} \end{bmatrix}$$

with:

$$h_{ij} = \begin{bmatrix} h_{ij}[0] & \cdots & h_{ij}[L-1] & 0 & \cdots & 0 \\ 0 & \ddots & \ddots & \ddots & \ddots & \vdots \\ \vdots & \ddots & \ddots & \ddots & \ddots & 0 \\ 0 & \cdots & 0 & h_{ij}[0] & \cdots & h_{ij}[L-1] \end{bmatrix}$$

where  $h_{ij}$  the action potential of the  $j^{th}$  motor unit recorded at the channel  $i$ . The noise in model A1 includes both electronic interference and the activity of motor units at the skin surface, depicted by low-energy action potentials that cannot be separated.

The linear instantaneous model in Equation A1 is inverted to retrieve the matrix of extended and spatially whitened sources. The inversion of the matrix is performed with an iterative gradient descent optimisation procedure with a contrast function that maximises the independence, or sparseness [43], of the estimated sources. This method extracts the motor neuron discharge timings associated with individual motor neurons and the unique representation of the associated multi-channel action potentials. The estimated sources are trains of delta functions centered at motor neuron activation instants, with varying amplitudes due to the estimation process. To separate the discharge timings from the baseline noise, K-Means clustering is applied to the estimated sources, comparing each candidate peak with the surrounding peaks.

Several blind source separation approaches have been proposed in the literature [13, 44–48]. However, these methods often struggle to separate sources when their waveforms are similar, resulting in overlapping signals. Current contrast functions and non-linear metrics are not optimised to resolve these overlaps. We thus utilised a novel algorithm, Swarm-Contrastive Decomposition (SCD) [42], that addresses these limitations by using an adaptive contrast function that enhances spike sorting accuracy by adapting to the unique characteristics of spiking distributions.

## Appendix B Lower-density configurations

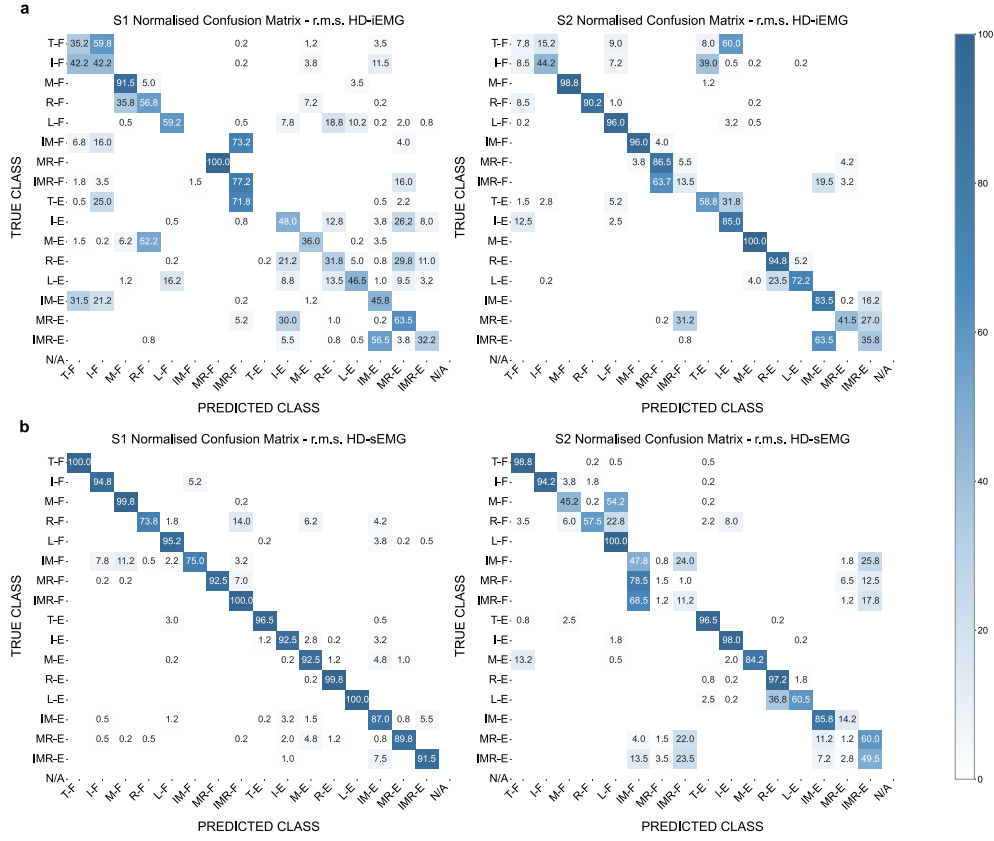


**Fig. B1** Normalised confusion matrices illustrating the percentage of predictions for each of the 12 flexion and extension gestures, comparing true labels (y-axis) with predicted labels (x-axis). The matrices show predictions for S1 on the left and S2 on the right, across different data types: **a** r.m.s. values of simulated bipolar, **b** r.m.s. values of 8-channel sEMG.



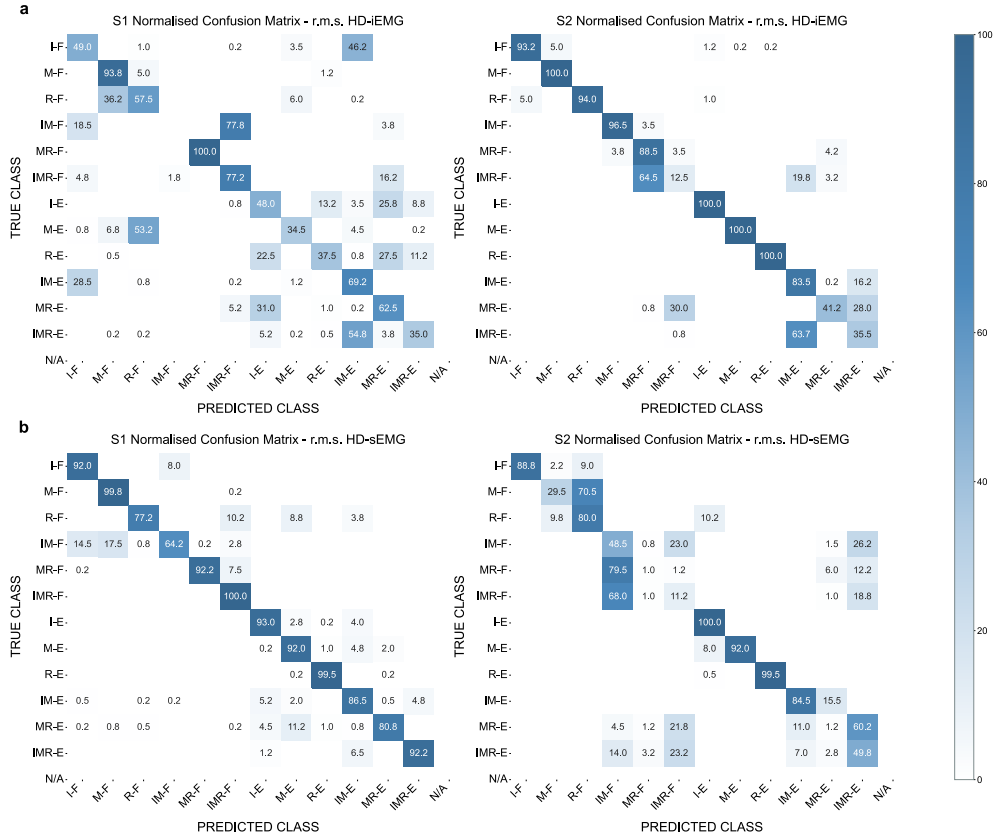


**Fig. B2** Normalised confusion matrices illustrating the percentage of predictions for each of the 12 flexion and extension gestures, comparing true labels (y-axis) with predicted labels (x-axis). The matrices show predictions for S1 on the left and Subject 2 (S2) on the right, across different data types: **a** time domain and r.m.s. values of simulated bipolar, **b** time domain and r.m.s. values of 8-channel sEMG.

## References

- [1] Hatsopoulos, N.G., Donoghue, J.P.: The science of neural interface systems. *Annual review of neuroscience* **32**(1), 249–266 (2009)
- [2] Lebedev, M.A., Nicolelis, M.A.: Brain–machine interfaces: past, present and future. *Trends in Neurosciences* **29**(9), 536–546 (2006)
- [3] Farina, D., Aszmann, O.: Bionic limbs: clinical reality and academic promises. *Science translational medicine* **6**(257), 257–1225712 (2014)
- [4] Oskoei, M.A., Hu, H.: Myoelectric control systems—a survey. *Biomedical signal processing and control* **2**(4), 275–294 (2007)
- [5] Zheng, M., Crouch, M.S., Eggleston, M.S.: Surface electromyography as a natural human–machine interface: a review. *IEEE Sensors Journal* **22**(10), 9198–9214 (2022)
- [6] Shenoy, P., Miller, K.J., Crawford, B., Rao, R.P.: Online electromyographic control of a robotic prosthesis. *IEEE Transactions on Biomedical Engineering* **55**(3), 1128–1135 (2008)
- [7] Wolczowski, A., Kurzyński, M.: Human–machine interface in bioprosthesis control using EMG signal classification. *Expert Systems* **27**(1), 53–70 (2010)
- [8] Farina, D., Vujaklija, I., Sartori, M., Kapelner, T., Negro, F., Jiang, N., Bergmeister, K., Andalib, A., Principe, J., Aszmann, O.C.: Man/machine interface based on the discharge timings of spinal motor neurons after targeted muscle reinnervation. *Nature biomedical engineering* **1**(2), 0025 (2017)
- [9] Mesin, L., Merletti, R., Rainoldi, A.: Surface EMG: the issue of electrode location. *Journal of Electromyography and Kinesiology* **19**(5), 719–726 (2009)
- [10] Muceli, S., Jiang, N., Farina, D.: Extracting signals robust to electrode number and shift for online simultaneous and proportional myoelectric control by factorization algorithms. *IEEE Transactions on Neural Systems and Rehabilitation Engineering* **22**(3), 623–633 (2014)
- [11] Farina, D., Merletti, R., Indino, B., Nazzaro, M., Pozzo, M.: Surface EMG crosstalk between knee extensor muscles: experimental and model results. *Muscle & Nerve: Official Journal of the American Association of Electrodiagnostic Medicine* **26**(5), 681–695 (2002)
- [12] Muceli, S., Poppendieck, W., Negro, F., Yoshida, K., Hoffmann, K.P., Butler, J.E., Gandevia, S.C., Farina, D.: Accurate and representative decoding of the neural drive to muscles in humans with multi-channel intramuscular thin-film electrodes. *The Journal of Physiology* **593**(17), 3789–3804 (2015)

- [13] Muceli, S., Poppendieck, W., Holobar, A., Gandevia, S., Liebetanz, D., Farina, D.: Blind identification of the spinal cord output in humans with high-density electrode arrays implanted in muscles. *Science advances* **8**(46), 5040 (2022)
- [14] Farina, D., Gandevia, S.: The neural control of movement: a century of in vivo motor unit recordings is the legacy of Adrian and Bronk. *The Journal of Physiology* **602**(2), 281–295 (2024)
- [15] Kashiwakura, J., Alva, P.G.S., Guerra, I.M., Bona, C., Atashzar, S.F., Farina, D.: Task-oriented design of a multi-degree of freedom upper limb prosthesis with integrated myocontrol and sensory feedback. *IEEE Transactions on Medical Robotics and Bionics* **5**(4), 1067–1081 (2023)
- [16] Toledo-Pérez, D.C., Rodríguez-Reséndiz, J., Gómez-Loenzo, R.A., Jauregui-Correa, J.: Support vector machine-based EMG signal classification techniques: A review. *Applied Sciences* **9**(20), 4402 (2019)
- [17] Bian, F., Li, R., Liang, P.: SVM based simultaneous hand movements classification using sEMG signals. In: 2017 IEEE International Conference on Mechatronics and Automation (ICMA), pp. 427–432 (2017). IEEE
- [18] Oßwald, M., Cakici, A.L., Oliveira, D.S.d., Braun, D.I., Del Vecchio, A.: Mechanical hand synergies during dynamic hand movements are mostly controlled in a non-synergistic way by spinal motor neurons. *bioRxiv*, 2023–07 (2023)
- [19] Farina, D., Merletti, R., Indino, B., Graven-Nielsen, T.: Surface EMG crosstalk evaluated from experimental recordings and simulated signals. *Methods of information in medicine* **43**(01), 30–35 (2004)
- [20] Mesin, L.: Crosstalk in surface electromyogram: literature review and some insights. *Physical and Engineering Sciences in Medicine* **43**, 481–492 (2020)
- [21] Farina, D., Merletti, R., Enoka, R.M.: The extraction of neural strategies from the surface EMG: an update. *Journal of applied physiology* **117**(11), 1215–1230 (2014)
- [22] Fajardo, J.M., Gomez, O., Prieto, F.: EMG hand gesture classification using handcrafted and deep features. *Biomedical Signal Processing and Control* **63**, 102210 (2021)
- [23] Simão, M., Neto, P., Gibaru, O.: EMG-based online classification of gestures with recurrent neural networks. *Pattern Recognition Letters* **128**, 45–51 (2019)
- [24] Jia, G., Lam, H.-K., Liao, J., Wang, R.: Classification of electromyographic hand gesture signals using machine learning techniques. *Neurocomputing* **401**, 236–248 (2020)

- [25] Chen, C., Yu, Y., Ma, S., Sheng, X., Lin, C., Farina, D., Zhu, X.: Hand gesture recognition based on motor unit spike trains decoded from high-density electromyography. *Biomedical signal processing and control* **55**, 101637 (2020)
- [26] Chen, C., Yu, Y., Sheng, X., Meng, J., Zhu, X.: Real-time hand gesture recognition by decoding motor unit discharges across multiple motor tasks from surface electromyography. *IEEE Transactions on Biomedical Engineering* **70**(7), 2058–2068 (2023)
- [27] Tanzarella, S., Iacono, M., Donati, E., Farina, D., Bartolozzi, C.: Neuromorphic decoding of spinal motor neuron behaviour during natural hand movements for a new generation of wearable neural interfaces. *IEEE Transactions on Neural Systems and Rehabilitation Engineering* **31**, 3035–3046 (2023)
- [28] Rossato, J., Hug, F., Tucker, K., Lacourpaille, L., Farina, D., Avrillon, S.: I-spin live: An open-source software based on blind-source separation for decoding the activity of spinal alpha motor neurons in real-time. *Elife* **12** (2023)
- [29] Chicca, E., Stefanini, F., Bartolozzi, C., Indiveri, G.: Neuromorphic electronic circuits for building autonomous cognitive systems. *Proceedings of the IEEE* **102**(9), 1367–1388 (2014)
- [30] Mead, C.: Neuromorphic Engineering: In Memory of Misha Mahowald. *Neural Computation* **35**, 343–383 (2023)
- [31] Guerra, I.M., Barsakcioglu, D.Y., Farina, D.: Adaptive EMG decomposition in dynamic conditions based on online learning metrics with tunable hyperparameters. *Journal of Neural Engineering* **21**(4), 046023 (2024)
- [32] Donati, E., Indiveri, G.: Neuromorphic bioelectronic medicine for nervous system interfaces: from neural computational primitives to medical applications. *Progress in Biomedical Engineering* **5**(1), 013002 (2023)
- [33] Jang, C.H., Yang, H.S., Yang, H.E., Lee, S.Y., Kwon, J.W., Yun, B.D., Choi, J.Y., Kim, S.N., Jeong, H.W.: A survey on activities of daily living and occupations of upper extremity amputees. *Annals of rehabilitation medicine* **35**(6), 907–921 (2011)
- [34] Carabello, A., Henkner, R., Drossel, W.-G.: Novel procedure for determining the finger force in flexion depending on the finger position. In: *Current Directions in Biomedical Engineering*, vol. 8, pp. 384–387 (2022). De Gruyter
- [35] Cort, J.A., Potvin, J.R.: Maximum isometric finger pull forces. *International Journal of Industrial Ergonomics* **41**(2), 91–95 (2011)
- [36] Oskoei, M.A., Hu, H.: Support vector machine-based classification scheme for myoelectric control applied to upper limb. *IEEE Transactions on Biomedical*

Engineering **55**(8), 1956–1965 (2008)

- [37] Purushothaman, G., Vikas, R.: Identification of a feature selection based pattern recognition scheme for finger movement recognition from multichannel EMG signals. *Australasian physical & engineering sciences in medicine* **41**, 549–559 (2018)
- [38] Dhindsa, I.S., Agarwal, R., Ryait, H.S.: Performance evaluation of various classifiers for predicting knee angle from electromyography signals. *Expert Systems* **36**(3), 12381 (2019)
- [39] Weir, R.F., Troyk, P.R., DeMichele, G.A., Kerns, D.A., Schorsch, J.F., Maas, H.: Implantable myoelectric sensors (IMESs) for intramuscular electromyogram recording. *IEEE Transactions on Biomedical Engineering* **56**(1), 159–171 (2008)
- [40] Merrill, D.R., Lockhart, J., Troyk, P.R., Weir, R.F., Hankin, D.L.: Development of an implantable myoelectric sensor for advanced prosthesis control. *Artificial organs* **35**(3), 249–252 (2011)
- [41] Salminger, S., Sturma, A., Hofer, C., Evangelista, M., Perrin, M., Bergmeister, K., Roche, A.D., Hasenoehrl, T., Dietl, H., Farina, D., *et al.*: Long-term implant of intramuscular sensors and nerve transfers for wireless control of robotic arms in above-elbow amputees. *Science Robotics* **4**(32), 6306 (2019)
- [42] Grison, A., Clarke, A.K., Muceli, S., Pereda, J.I., Kundu, A., Farina, D.: A particle swarm optimised independence estimator for blind source separation of neurophysiological time series. *IEEE Transactions on Biomedical Engineering* (2024)
- [43] Negro, F., Muceli, S., Castronovo, A.M., Holobar, A., Farina, D.: Multi-channel intramuscular and surface EMG decomposition by convolutive blind source separation. *Journal of neural engineering* **13**(2), 026027 (2016)
- [44] Jäckel, D., Frey, U., Fiscella, M., Franke, F., Hierlemann, A.: Applicability of independent component analysis on high-density microelectrode array recordings. *Journal of neurophysiology* **108**(1), 334–348 (2012)
- [45] Leibig, C., Wachtler, T., Zeck, G.: Unsupervised neural spike sorting for high-density microelectrode arrays with convolutive independent component analysis. *Journal of neuroscience methods* **271**, 1–13 (2016)
- [46] Buccino, A.P., Hagen, E., Einevoll, G.T., Häfliger, P.D., Cauwenberghs, G.: Independent component analysis for fully automated multi-electrode array spike sorting. In: 2018 40th Annual International Conference of the IEEE Engineering in Medicine and Biology Society (EMBC), pp. 2627–2630 (2018). IEEE
- [47] Chen, M., Zhou, P.: 2CFastICA: A novel method for high density surface EMG

decomposition based on kernel constrained fastICA and correlation constrained fastICA. *IEEE Transactions on Neural Systems and Rehabilitation Engineering* **32**, 2177–2186 (2024)

- [48] Chen, M., Zhang, X., Zhou, P.: Automatic multichannel intramuscular electromyogram decomposition: progressive fastICA peel-off and performance validation. *IEEE Transactions on Neural Systems and Rehabilitation Engineering* **27**(1), 76–84 (2019)